The hydrogen evolution and oxidation kinetics during overdischarging of sealed nickel-metal hydride batteries

Journal of The Electrochemical Society, **153** (11) A2055-A2065 (2006)
0013-4651/2006/153(11)/A2055/11/$20.00 © The Electrochemical Society

The Hydrogen Evolution and Oxidation Kinetics during Overdischarging of Sealed Nickel-Metal Hydride Batteries

A. Ayeb,[a] W. M. Otten,[a] A. J. G. Mank,[b] and P. H. L. Notten[a,b,*]

[a]*Eindhoven University of Technology, 5600 MB Eindhoven, The Netherlands*
[b]*Philips Research Laboratories, 5656 AA Eindhoven, The Netherlands*

The hydrogen evolution and oxidation kinetics in NiMH batteries have been investigated under temperature-controlled, steady-state, overdischarging conditions within a temperature range of 10 and 50°C and at discharging currents of 1–330 mA (0.0009 to 0.3 C rate). In situ Raman spectroscopic analyses of the gas phase showed that hydrogen is the only gas evolving inside the battery during overdischarge at the above-mentioned conditions. The pressure increase could be very critical at low temperatures, leading to opening of the safety vent at relatively low discharging currents, for example, only 220 mA at 10°C. The polarization parameters for the hydrogen evolution reaction, such as Tafel slopes and exchange currents were determined at the different temperatures as well as the activation energy for the evolution and oxidation processes. The reaction mechanisms and the rate-determining steps are discussed. These are highly valuable information in NiMH modeling as they are obtained directly from the system of interest. Furthermore, the obtained results make battery simulations more realistic by minimizing the number of parameters involved and making the correct assumptions.
 [DOI: 10.1149/1.2336993]

Manuscript submitted March 17, 2006; revised manuscript received May 8, 2006. Available electronically September 8, 2006.

The sealed rechargeable nickel metal hydride battery (NiMH) is one of the latest developments in battery technologies.[1] These batteries are widely used in a growing number of wireless electronic products and nowadays successfully applied in hybrid electrical vehicles (HEVs) to assist in fuel savings and lower emissions in the modern-day automotive market.[2-4] The main advantages of NiMH batteries are their environmental friendliness and high energy density. Their capacity is 50% more than that of NiCd batteries and they are strong competitors for the Li-ion batteries regarding safety, cost performance, and cycle life.[2]

For a sealed rechargeable system, the internal pressure increase during overcharge and overdischarge should, however, be kept to a minimum. So any reaction that may lead to gas generation should be avoided or well controlled. When these reactions are inevitable, the battery design should take into account a gas recombination cycle allowing the gas formation at one electrode and consumption at the other electrode. In the NiMH battery system, this could be achieved by choosing the appropriate ratio of the electrodes capacities. Unfortunately, this does not completely solve the problem and the battery internal pressure was found to reach limiting values leading to the opening of the safety vent for different reasons, such as severe abuse of the battery, when the battery presents some manufacturing defects and/or when using a number of batteries having different capacities in series, which is of special importance in large scale applications like HEV.

This paper is devoted to the gas generation and consumption reactions during the overdischarge of NiMH batteries. The case of the overcharge will be addressed in a separate paper in the near future.

During normal battery charging (ch) and discharging (d) the main electrochemical reactions can be represented by[5,6]

$$x\mathrm{NiOOH} + x\mathrm{H_2O} + x\mathrm{e^-} \underset{\text{ch}}{\overset{\text{d}}{\rightleftarrows}} x\mathrm{Ni(OH)_2} + x\ \mathrm{OH^-} \qquad [1]$$

at the nickel hydroxide electrode (Ni) and

$$\mathrm{MH}_x + x\ \mathrm{OH^-} \underset{\text{ch}}{\overset{\text{d}}{\rightleftarrows}} \mathrm{M} + x\mathrm{H_2O} + x\mathrm{e^-} \qquad [2]$$

at the metal hydride electrode (MH). In addition to the above main electrochemical reactions, reactions leading to O_2 and H_2 generation may take place at the nickel electrode, as this is the capacity-limiting electrode in the NiMH battery, during overcharge and overdischarge, respectively. The complete reactions scheme inside the NiMH battery for the charge/overcharge and discharge/overdischarge processes is represented in Fig. 1.[5]

During overdischarge, the hydrogen evolution (her) and oxidation (hor) reactions in alkaline solution are given in the following equations.[5,6] At the Ni electrode the overall reaction is

$$2\mathrm{H_2O} + 2\mathrm{e^-} \underset{k^a_{\mathrm{Ni}}}{\overset{k^c_{\mathrm{Ni}}}{\rightleftarrows}} 2\ \mathrm{OH^-} + \mathrm{H_2} \qquad [3]$$

and at the MH electrode

$$2\ \mathrm{OH^-} + \mathrm{H_2} \underset{k^c_{\mathrm{MH}}}{\overset{k^a_{\mathrm{MH}}}{\rightleftarrows}} 2\mathrm{H_2O} + 2\mathrm{e^-} \qquad [4]$$

where k^a_{Ni} and k^c_{Ni} are the rate constants for the anodic and cathodic directions of the her at the Ni electrode, respectively, and k^a_{MH} and k^c_{MH} are those for the hor at the MH electrode.

Equation 3 represents the overall reaction of the hydrogen evolution reaction (her) at the Ni electrode. Usually, this reaction occurs in multiple steps, representing two competitive mechanisms and the rate-determining step (rds) is still a subject of debate. It is generally agreed that these two mechanisms are the Volmer–Heyrovsky mechanism (given by Eq. 5 and 6) and the Volmer–Tafel mechanism (given by Eq. 5 and 7)[7-10]

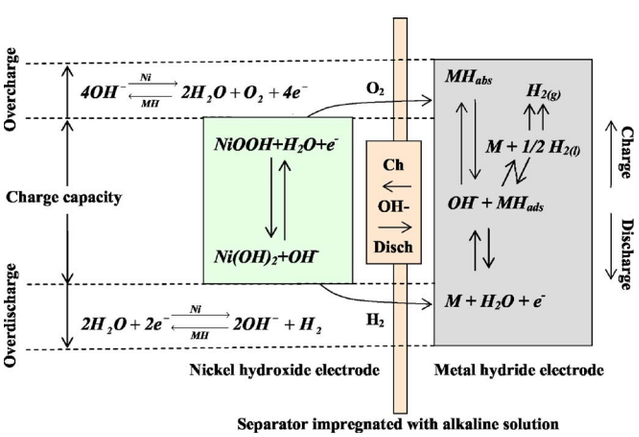

Figure 1. (Color online) Schematic representation of the main electrochemical storage reactions and side reactions inside a NiMH battery.

* Electrochemical Society Active Member.

$$H_2O + e^- \underset{k_{-1}}{\overset{k_1}{\rightleftarrows}} H_{(ad)} + OH^- \text{ (Volmer)} \quad [5]$$

$$H_2O + e^- + H_{(ad)} \underset{k_{-2}}{\overset{k_2}{\rightleftarrows}} H_2 + OH^- \text{ (Heyrovsky)} \quad [6]$$

$$H_{(ad)} + H_{(ad)} \underset{k_{-3}}{\overset{k_3}{\rightleftarrows}} H_2 \text{ (Tafel)} \quad [7]$$

where k_j and k_{-j} are the rate constants for the forward and backward directions, respectively. The first step (Eq. 5), known as the Volmer reaction, is the primary electron transfer step, resulting in the formation of adsorbed hydrogen (H_{ad}) at the electrode surface. It is followed by the second step (Eq. 6) or/and the third step (Eq. 7) to complete the her. Reaction 6, known as the Heyrovsky reaction, shows the formation of H_2 molecules by desorption of adsorbed hydrogen and a simultaneous reduction of a H_2O molecule. Reaction 7, generally denoted as the Tafel reaction, reveals the formation of H_2 molecules by recombination of two neighboring surface hydrogen atoms. As the two mechanisms of hydrogen evolution can occur in parallel, the overall reaction rate of the hydrogen evolution reaction will be determined by the slowest step in the fastest mechanism. Note that when the rds is the Volmer reaction, it is difficult to determine whether the Heyrovsky or the Tafel step follows and, consequently, the mechanism of the her at the nickel electrode will still remain a question.

A survey of the literature showed that a large number of studies of the her concerns nickel surfaces and/or alloys containing Ni as they present very good catalysts for hydrogen production systems.[11-35] Ni-hydroxide electrodes were not extensively studied. However, Chialvo et al.[11] and Salgado et al.[12] demonstrated that the her at Ni metal surfaces in alkaline solutions proceeds on a thin nickel-hydroxide overlayer. Most of the authors, who studied the her on metal surfaces containing Ni, demonstrated that the Volmer-Heyrovsky mechanism is more appropriate to describe the her.[13-23] Furthermore, the Heyrovsky step was shown to be the rds in most of the cases. However some deviations were encountered showing that the her kinetics could be potential-dependent; Daojun et al. showed that the Volmer step can be the rds at high overpotentials on amorphous Ni-Mo-Fe-Zn coatings.[23] Krstajic et al. showed that the Tafel reaction can be the rds at low overpotentials while the Heyrovsky step becomes the rds at higher overpotentials on Nickel-Sulfur electrodes.[24]

The hydrogen oxidation reaction (hor) occurs at the MH electrode via Reaction 4. The evolved hydrogen at the nickel electrode and dissolved in the electrolyte is transported to the MH electrode surface where it dissociates to adsorbed hydrogen atoms which subsequently oxides to form water molecules. Compared to the relative abundance of studies concerning the her, only a few studies are available concerning the hor.[36-41] The opposite path of the mechanism of her (Eq. 5-7) generally holds for the hor. However, the kinetic parameters and the rds can be different to that of the her especially in the present case where these reactions occur at different electrodes surfaces. A diffusion limitation could be envisaged because hydrogen molecules have to diffuse through the electrolyte to the MH electrode surface where they are oxidized.

In the present paper, the kinetics of the her at the Ni electrode and those of the hor at the MH electrode during overdischarge were in situ investigated inside rechargeable NiMH batteries as a function of temperature. Galvanostatic potentiometry under steady state conditions combined with in situ Raman spectroscopic analyses of the gas phase, to determine the gas phase composition, was used to obtain information on the studied reactions.

Theoretical Considerations

During normal discharging conditions, the current applied to the battery (I) is used to reduce the nickeloxyhydroxide to the nickel-hydroxide (Reaction 1) and no hydrogen generation should be observed. When the battery is being completely discharged and the potential is sufficiently negative (prolonged overdischarge), the her starts at the Ni electrode and then the current (I) is completely used to drive the her. Considering that the capacity of the MH electrode is substantially larger than that of the Ni electrode, Reaction 2 may still take place together with the hor, so the following equation describing the current distribution is obtained

$$I = I_{\text{her,Ni}} = I_{\text{MH}} + I_{\text{hrr,MH}} \quad [8]$$

where I_{MH} is the current for the main reaction at the MH electrode (Reaction 2). $I_{\text{her,Ni}}$ is the current of H_2 evolution at the Ni electrode, and $I_{\text{hor,MH}}$ the current of H_2 oxidation at the MH electrode.

Using Faraday's law, the accumulation rate of hydrogen, dm_{H_2}/dt where m_{H_2} is the molar amount of hydrogen in both the gas phase and dissolved in the electrolyte, is related to the rate of H_2 production at the Ni electrode ($I_{\text{her,Ni}}$) and the rate of H_2 oxidation at the MH electrode ($I_{\text{hor,MH}}$) via

$$\frac{dm_{H_2}}{dt} = \frac{I_{\text{her,Ni}} - I_{\text{hor,MH}}}{2F} \quad [9]$$

The molar amount of hydrogen, which is the molar amount in the gas phase plus that dissolved in the electrolyte cannot be directly measured and should be expressed in terms of more accessible quantities, such as pressure. In fact, the gas law represents the relationship between the partial hydrogen pressure (P_{H_2}), the number of moles of hydrogen in the gas phase ($m_{H_2(g)}$), the battery temperature (T) and the free gas volume (V_g) inside the battery, according to

$$m_{H_2(g)} = \frac{p_{H_2} V_g}{RT} \quad [10]$$

The number of moles of hydrogen in the electrolyte ($m_{H_2(l)}$) is obtained from the expression of the hydrogen activity in the liquid phase ($a_{H_2(l)}$)

$$a_{H_2(l)} = \gamma_{H_2(l)} \times \frac{m_{H_2(l)}}{V_l} \quad [11]$$

where $\gamma_{H_2(l)}$ is the activity coefficient of the dissolved hydrogen in the electrolyte and V_l is the electrolyte volume. Assuming that hydrogen is an ideal gas, then its activity in the liquid phase is proportionally related to its fugacity in the gas phase by Henry's law ($a_{H_2(l)} = K^H_{H_2} f_{H_2(g)}$)[42] and hence directly proportional to its partial pressure (as $f_{H_2(g)} = \gamma_{H_2(g)} p_{H_2}$, according to

$$a_{H_2(l)} = k_{H_2} p_{H_2} \quad [12]$$

in which $k_{H_2} = K^H_{H_2} \times \gamma_{H_2(g)}$, $K^H_{H_2}$ is Henry's constant and $\gamma_{H_2(g)}$ is the fugacity coefficient. Using Eq. 12 to express the hydrogen activity in the liquid phase in Eq. 11 leads to an expression of the molar amount of the dissolved hydrogen in the electrolyte as a function of the hydrogen partial pressure

$$m_{H_2(l)} = \frac{V_l k_{H_2} p_{H_2}}{\gamma_{H_2(l)}} \quad [13]$$

As a result the total molar amount of hydrogen is obviously

$$m_{H_2} = m_{H_2(g)} + m_{H_2(l)} = \left(\frac{V_g}{RT} + \frac{V_l k_{H_2}}{\gamma_{H_2(l)}} \right) p_{H_2} \quad [14]$$

Equation 14 shows that the total molar amount of hydrogen is proportional to its partial pressure. The time derivative of Eq. 14 gives

$$\frac{dm_{H_2}}{dt} = \left(\frac{V_g}{RT} + \frac{V_l k_{H_2}}{\gamma_{H_2(l)}} \right) \frac{dp_{H_2}}{dt} \quad [15]$$

Equation 15 reveals that a constant hydrogen partial pressure during galvanostatic overdischarge is an indication of the establishment of a steady state condition. Replacing $\frac{dm_{H_2}}{dt}$ in Eq. 9 by means of Eq. 14 leads to a general expression for the hydrogen pressure build up inside the NiMH battery

$$\frac{dp_{H_2}}{dt} = \left(\frac{RT\gamma_{H_2(l)}}{V_g\gamma_{H_2(l)+RTV_l k_{H_2}}} \right) \frac{I_{her,Ni} - I_{hor,MH}}{2F} \quad [16]$$

A special case can now be considered when the applied current to the battery is entirely used to drive the hydrogen evolution and oxidation cycle. Under these steady state overdischarging conditions

$$\frac{dp_{H_2}}{dt} = 0 \quad \text{and} \quad I_{MH} = 0$$

Equation 16 then reduces to

$$I_{her,Ni} = I_{hor,MH} = I \quad [17]$$

From Eq. 17, one can see that steady-state overdischarging experimental conditions yields valuable and simultaneous information on both the her and hor kinetics. The steady state method was also successfully used by Notten et al.[42] to study the oxygen evolution recombination cycle for the NiCd battery. Due to its simplicity it is a very elegant method to study both reactions mechanisms simultaneously.

The hydrogen evolution reaction (her).— Under Tafel conditions $\left(-\eta \gg \frac{RT}{F}\right)$, the kinetic equation of the her at the Ni electrode can be written as

$$I_{her,Ni} = I^0_{H_2,Ni} \exp\left(-(1-\alpha_{her})\frac{nF}{RT}\eta_{her} \right) = I^0_{H_2,Ni} \exp\left(\frac{-2.3 \times \eta_{her}}{b_{her}} \right) \quad [18]$$

where $I_{her,Ni}$ is the hydrogen evolution current corresponding to an overpotential $\eta_{her}(\eta_{her} = E_{Ni} - E^{eq}_{H_2})$, E_{Ni} is the nickel electrode potential, $E^{eq}_{H_2}$ the reversible potential of the her, $I^0_{her,Ni}$ the exchange current, α_{her} the charge transfer coefficient for the her at the nickel electrode. n, F, R, and T have their usual meaning. b_{her} is called the Tafel slope and is an indication of the rds as was explained by Lefebvre.[43] $I^0_{her,Ni}$ has the following expression

$$I^0_{her,Ni} = nFA_{Ni}(k^a_{Ni})^{(1-\alpha_{her})}(k^c_{Ni})^{\alpha_{her}} a^{(1-\alpha_{her})x_{her}}_{H_2(l)} a^{\alpha_{her} y_{her}}_{OH^-} a^{\alpha_{her} z_{her}}_{H_2O} \quad [19]$$

where x, y, and z are the her reaction orders for H_2, OH^-, and H_2O, respectively. The reversible potential of the her is obtained by[42]

$$E^{eq}_{H_2} = E^{eq,ref}_{H_2}(T) + \frac{RT}{nF} \ln\left(\frac{a^{x_{her}}_{H_2,ref}}{a^{x_{her}}_{H_2(l)}} \times \frac{a^{z_{her}}_{H_2O} a^{y_{her}}_{OH^-,ref}}{a^{y_{her}}_{OH^-} a^{z_{her}}_{H_2O,ref}} \right) \quad [20]$$

where $E^{eq,ref}_{H_2}$ is the equilibrium redox potential of the her at T vs a chosen reference hydrogen activity. Considering the water and the hydroxyl ions activities as constants (concentrated electrolyte), defining the reference hydrogen partial pressure at 1 bar and using Eq. 12 to express the hydrogen activity, Eq. 20 transforms into

$$E^{eq}_{H_2} = E^0_{H_2}(T) + \frac{RT}{nF} \ln\left(\frac{a_{H_2,ref}}{a_{H_2(l)}} \right)^{x_{her}} = E^0_{H_2}(T) + \frac{RT}{nF} \ln\left(\frac{1}{p_{H_2}} \right)^{x_{her}} \quad [21]$$

where $E^0_{H_2}(T)$ is the reference redox potential of the her at T and a reference state of $p_{H_2,ref}$ of 1 bar and an electrolyte concentration of 8.47 M. It is equal to −0.870 V vs the Hg/HgO reference electrode at 25°C with a temperature coefficient of −0.836 mV/K. The temperature coefficient of the standard redox potential of the reference electrode is −1.125 mV/K. Replacing the overpotential in Eq. 18 by its expression, $\eta_{her} = E_{Ni} - E^{eq}_{H_2}$ and expressing the equilibrium potential by Eq. 20, Eq. 18 can be rewritten as

$$I_{her,Ni} = I^0_{her,Ni} \left(\frac{a_{H_2(l)}}{a_{H_2,ref}} \right)^{-(1-\alpha_{her})x_{her}} \exp\left\{ -(1-\alpha_{her})\frac{nF}{RT}(E_{Ni} - E^0_{H_2}(T)) \right\} \quad [22]$$

Introducing the expression of the exchange current (Eq. 19) in Eq. 22, we obtain

$$I_{her,Ni} = nFA_{Ni}(k^a_{Ni})^{(1-\alpha_{her})}(k^c_{Ni})^{\alpha_{her}} a^{(1-\alpha_{her})x_{her}}_{H_2,ref} a^{(1-\alpha_{her})y_{her}}_{OH^-} a^{\alpha_{her} z_{her}}_{H_2O} \times \exp\left(-(1-\alpha_{her})\frac{nF}{RT}(E_{Ni} - E^0_{H_2}(T)) \right) \quad [23]$$

Comparing the pre-exponential product to Eq. 19, one can see that it represents the exchange current for the her at the Ni electrode at the reference state, $I^{0,ref}_{her,Ni}$, so Eq. 23 can be simply rewritten as

$$I_{her,Ni} = I^{0,ref}_{her,Ni} \exp\left(-(1-\alpha_{her})\frac{nF}{RT}(E_{Ni} - E^0_{H_2}(T)) \right) \quad [24a]$$

or in the logarithm form as

$$\ln(I_{her,Ni}) = \ln(I^{0,ref}_{her,Ni}) - (1-\alpha_{her})\frac{nF}{RT}(E_{Ni} - E^0_{H_2}(T)) \quad [24b]$$

Equation 24 reveals that the her kinetics are independent of the hydrogen partial pressure.

The hydrogen oxidation reaction (hor).— Two cases will be considered: kinetically-controlled hor and diffusion controlled hor.

For a purely kinetically-controlled hydrogen oxidation reaction, for which no transport limitations have to be considered, the partial oxidation current ($I_{hor,MH}$) can be expressed by the Butler-Volmer equation

$$I_{hor,MH} = I^0_{hor,MH}\left[\exp\left(\alpha_{hor}\frac{nF\eta_{hor}}{RT} \right) - \exp\left(-(1-\alpha_{hor})\frac{nF\eta_{hor}}{RT} \right) \right] \quad [25]$$

where η_{hor} ($\eta_{hor} = E_{MH} - E^{eq}_{H_2}$) is the overpotential at the MH electrode. α_{hor} and $I^0_{hor,MH}$ are the charge transfer coefficient and the exchange current for the hor at the MH electrode, respectively. A similar equation to Eq. 19 can be derived for the exchange current, $I^0_{hor,MH}$

$$I^0_{hor,MH} = nFA_{MH}(k^c_{MH})^{\alpha_{hor}}(k^a_{MH})^{(1-\alpha_{hor})} a^{(1-\alpha_{hor})x_{hor}}_{H_2(l)} a^{(1-\alpha_{hor})y_{hor}}_{OH^-} a^{\alpha_{hor} z_{hor}}_{H_2O} \quad [26]$$

When the overpotential at the metal hydride electrode is relatively large so that Tafel conditions hold, the second exponential term in Eq. 25 can be neglected

$$I_{hor,MH} = I^0_{hor,MH} \exp\left(\alpha_{hor}\frac{nF\eta_{hor}}{RT} \right) \quad [27]$$

Introducing $E_{MH} - E^{eq}_{H_2}$ in Eq. 29, replacing $E^{eq}_{H_2}$ by using Eq. 21, which also holds for the oxidation reaction, and using Eq. 12 for hydrogen activity, the following expression is obtained for the hydrogen oxidation current at the metal hydride electrode

$$I_{hor,MH} = I^{0,ref}_{hor,MH} \left(\frac{p_{H_2}}{p^{ref}_{H_2}} \right)^{x_{hor}} \exp\left(\alpha_{hor}\frac{nF}{RT}\left(E_{MH} - E^0_{H_2}(T)\right) \right) \quad [28]$$

where

$$I^{0,ref}_{hor,MH} = nFA_{MH}(k^c_{MH})^{\alpha_{hor}}(k^a_{MH})^{(1-\alpha_{hor})} a^{(1-\alpha_{hor})x_{hor}}_{H_2,ref} a^{(1-\alpha_{hor})y_{hor}}_{OH^-} a^{\alpha_{her} z_{hor}}_{H_2O} \quad [29]$$

Plotting the logarithmic form of Eq. 28 gives

$$\ln I_{\text{hor},MH} = \ln(I^{0,\text{ref}}_{\text{hor,MH}}) + x_{\text{hor}}\ln\left(\frac{p_{H_2}}{P_{H_2,\text{ref}}}\right) + \left(\alpha_{\text{hor}}\frac{nF}{RT}(E_{\text{MH}} - E^0_{H_2}(T))\right) \quad [30]$$

Unlike the her, Eq. 30 shows that the hor kinetics are dependent on the hydrogen partial pressure.

For a purely diffusion controlled hor and assuming that a linear concentration gradient is established across the diffusion layer thickness, the oxidation rate can be described by

$$I_{\text{hor,MH}} = \frac{nFA_{\text{MH}}D_{H_2}}{\gamma_{H_2}d_{H_2}}(a_{H_2(l)} - a_{H_2(s)}) \quad [31]$$

where D_{H_2} is the diffusion coefficient for H_2 in the electrolyte and d_{H_2} the average diffusion layer thickness, through which H_2 must be transported to the interface. $a_{H_2(l)}$ and $a_{H_2(s)}$ are the activities of hydrogen in the bulk of the electrolyte and at the surface of the electrode, respectively. When the oxidation rate is completely dominated by mass transport, $a_{H_2(s)}$ at the electrode surface equals zero and the diffusion-controlled oxidation current can be reduced to

$$I_{\text{hor,MH}} = \frac{nFA_{\text{MH}}D_{H_2}}{\gamma_{H_2(l)}d_{H_2}}a_{H_2(l)} \quad [32]$$

Using Eq. 12, Eq. 32 is converted into

$$I_{\text{hor,MH}} = K^{\text{d}}_{\text{hm}}p_{H_2} \quad [33]$$

where

$$K^{\text{d}}_{\text{hor}} = \frac{nFA_{\text{MH}}D_{H_2}k_{H_2}}{\gamma_{H_2(l)}d_{H_2}} \quad [34]$$

is a constant that will be denoted as the diffusion oxidation constant. Comparing Eq. 30 and 33, one can see that for a first order reaction towards hydrogen and when the MH electrode potential is relatively constant, it is not possible to distinguish between diffusion- and kinetic-controlled reactions. However, when the reaction order deviates from Reaction 1, the kinetics may become the controlling process.

Experimental

All of the experiments were performed with commercial AA size NiMH batteries of the type HHR110AAOK (Matsushita Battery Industries, Japan). The nominal battery capacity is about 1100 mAh at room temperature. Two experimental setups were used for this study: a closed setup and an open battery setup.

For the closed battery setup, a hole (Φ = 0.5 mm) was drilled in the bottom of the battery. Subsequently, the battery was placed in a special holder to ensure electrical connections and a gastight connection to a pressure sensor, as shown in Fig. 2. A pre-calibrated thermocouple was pasted to the battery to monitor the battery temperature. The whole setup was then placed in a temperature controlled chamber. The temperature was controlled by means of a thermostat (HAAKE C25P, Thermo Electron Corporation) within the temperature range of 10–50°C. The battery voltage, temperature, and internal pressure were measured during the experiments.

For the open battery setup, the positive battery cap of the housing was removed and the open battery was placed in a double-walled glass vessel, allowing temperature control. The battery was fully immersed in extra electrolyte with the same composition and concentration as that inside the battery (Fig. 3). The reference electrode (Hg/HgO, 8.5 M alkaline solution) was placed as close as possible to the open top of the battery to minimize the ohmic losses. The open battery setup allows the measurement of individual electrode potentials.

The internal resistance (R) was determined for both the battery and electrodes at different temperatures, using the current-interruption method. In this paper, all of the measured potentials were corrected for the internal resistance. Electrochemical measurements were performed using Maccor Systems (Tulsa, OK). The galvanostatic method was applied in all experiments.

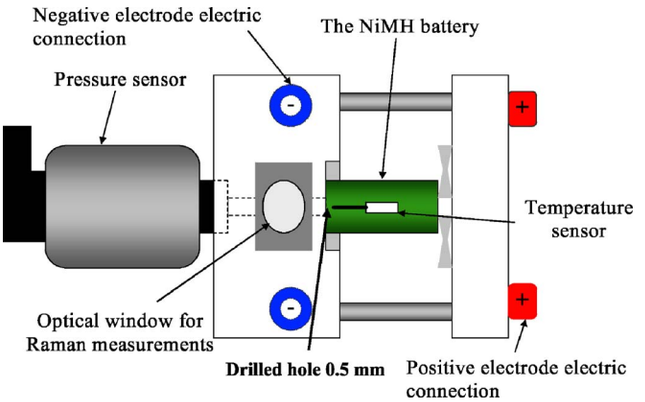

Figure 2. (Color online) Schematic presentation of the closed battery setup.

Prior to all experiments, the battery was activated according to a standard activation procedure to ensure battery stability and hence to increase the reproducibility of the experiments and to minimize the differences between the various batteries. The activation procedure consisted of five cycles, each consisting of the following steps: charging with 0.55 A for 150 min followed by a rest period of 1 h then discharging with −0.55 A, a rest period of 15 min, additionally discharging with −0.11 A followed by a final rest period of 15 min. The discharge steps were terminated at a battery cutoff voltage (E_{NiMH}) of 0.9 V or at a Ni electrode cutoff potential of 0 V vs Hg/HgO, depending on which potential is measured.

To determine the exact gas composition during the overdischarging process, gas phase analyses are necessary. For this purpose, in situ Raman microscopy was chosen and adapted for gas analyses during closed battery operation. The method was described in detail in a previous paper.[44]

Results and Discussion

A conventional charge and discharge cycle of a NiMH battery is shown in Fig. 4a. After charging (a) and discharging (c) the battery is allowed to equilibrate during the resting periods (b and c) when the current is switched off. Deep-discharging with a low current is

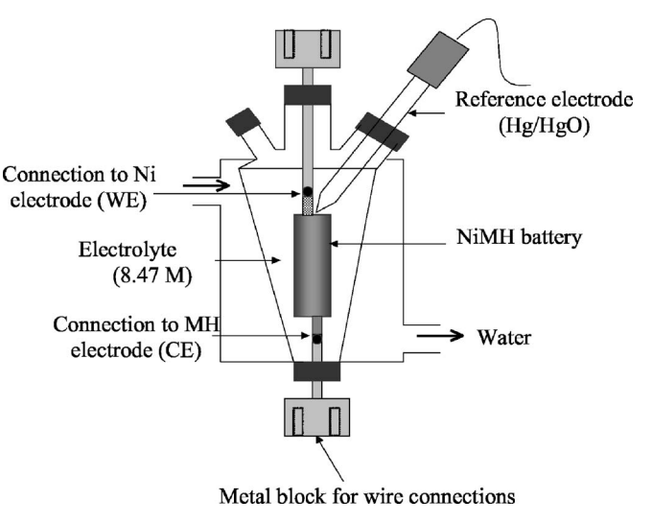

Figure 3. Schematic presentation of the open battery setup.

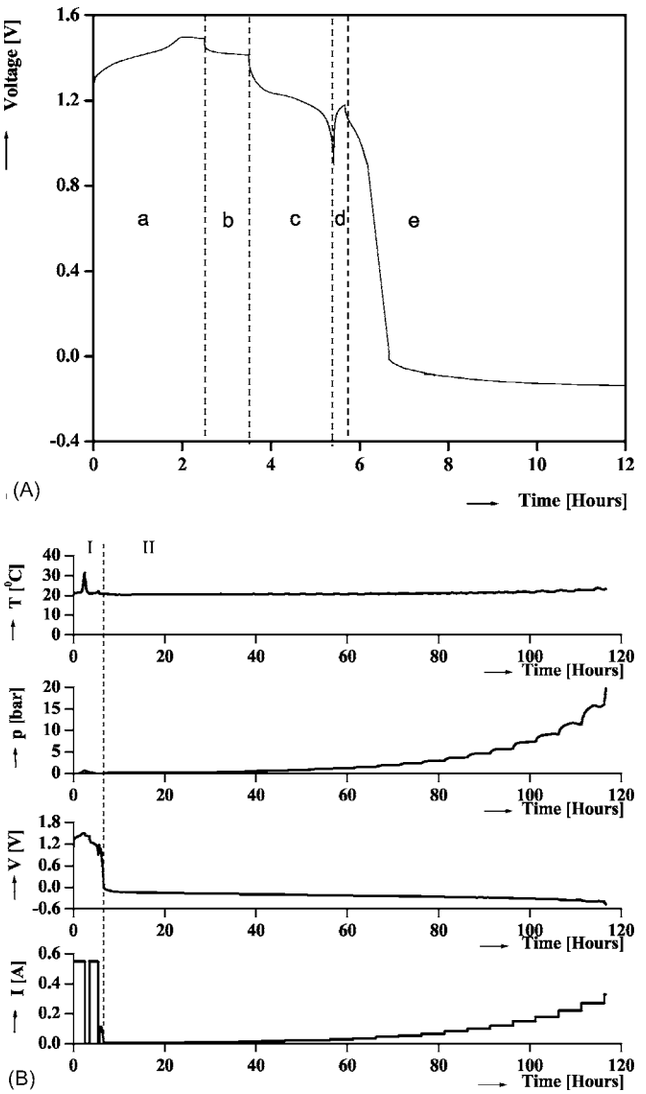

Figure 4. (A) (a) Constant current (0.55 A) charging, (b) 1 h resting, (c) constant current (0.55 A) discharging, and (d) 15 min resting of an AA size (HHR110AAOK-type) NiMH battery. (e) Low current (0.11 A) deep discharging induced until the steady state is attained. (B) Measurements of the pressure *P*, voltage *V*, and temperature *T*, during overdischarging at various currents in the closed battery setup.

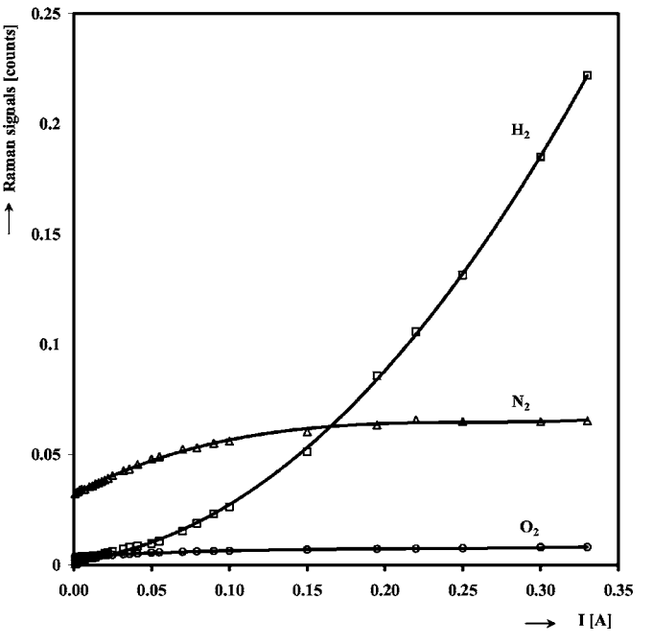

Figure 5. Raman spectroscopy results of the analysis of the gas phase at different overdischarging currents in the closed battery setup at 20°C.

commenced at (e). It can be seen that the battery voltage slowly drops to lower values. Under normal battery operating condition this deep-discharging process is terminated at about 0.9 V. In our experiments, however, deep-discharging was continued with a low current until a steady-state situation was attained at negative potentials.

The kinetics of the hydrogen evolution and oxidation reactions was investigated under these continuously overdischarging conditions by changing the overdischarging current, as shown in Fig. 4b. The applied current ranged between 0.001 and 0.33 A. The stabilization time needed to attain a steady state depends on the applied current. However, a period of 4–6 h was found to be sufficient for all the tested currents. Figure 4b reveals that fully discharged NiMH batteries can be overdischarged to a large extent under ambient temperature-controlled conditions without a clear variation of its temperature, contrarily to the case of overcharging.[5] This is essential for proper kinetic investigations of the hydrogen evolution and oxidation reactions. The maximum allowed overdischarging current is limited by two factors: on the one hand, the maximum pressure built up without causing the safety vent to open and, on the other hand, that no oxygen evolution reaction takes place at the MH electrode.

The Raman microscopic analysis of the gas phase during the overdischarging experiment at 20°C is shown in Fig. 5. It is obvious from the variation in the analyzed gas signals that hydrogen is the most important evolved gas. The Raman signals are converted to partial pressure in Fig. 6a. The variation in nitrogen signal is attributed to the change in the free gas volume of the battery.[44] The battery free gas volume was determined using the nitrogen partial pressure and the gas law and used to determine the molar amount of the different gases. The molar amounts of the various gases are represented in Fig. 6b. It is clear from Fig. 6b, that hydrogen is the sole gas evolving inside the battery. Similar results are obtained at the other investigated temperatures.

The hydrogen evolution reaction (her).— To investigate the kinetics of the her, the polarization curves of the Ni electrode measured against the Hg/HgO reference electrode are plotted. Figure 7 shows the applied current vs $E_{Ni} - E^0_{H_2}(T)$ on a semi-logarithmic scale (see Eq. 24b). Two well-defined linear regions are found at all temperatures: region I at low currents and region II at high currents. The polarization parameters obtained for the her on the nickel electrode for both Tafel regions are collected in Table I.

This behavior of the her at the Ni electrode was also observed by other authors.[34-36] Kibria et al.[27] found two Tafel regions with slopes of 80 and 160 mV/dec. However, other authors reported a single Tafel region with large spreads in the experimentally determined slopes ranging from 60 to more than 120 mV/dec.[25-32] A slope close to 116 mV/dec was also observed at many other metal surfaces. Examples of exception are Pd and Pt for which the slope is 30 mV/dec while for Rh and W, slopes of about 60 mV/decade were reported.[7]

Different explanations were reported to describe the appearance of multi-Tafel regions within a polarization curve. First, a change of the rds in a mechanism composed of successive reactions.[37,42] Erdey-Gruz et al. showed that a change of the rds in a sequence of consecutive steps will change the slope of the polarization curve differently than for a change of the rds in a sequence of parallel steps.[8] Second, it was shown that one rds could have two Tafel regions with extreme surface coverage of adsorbed atoms (when

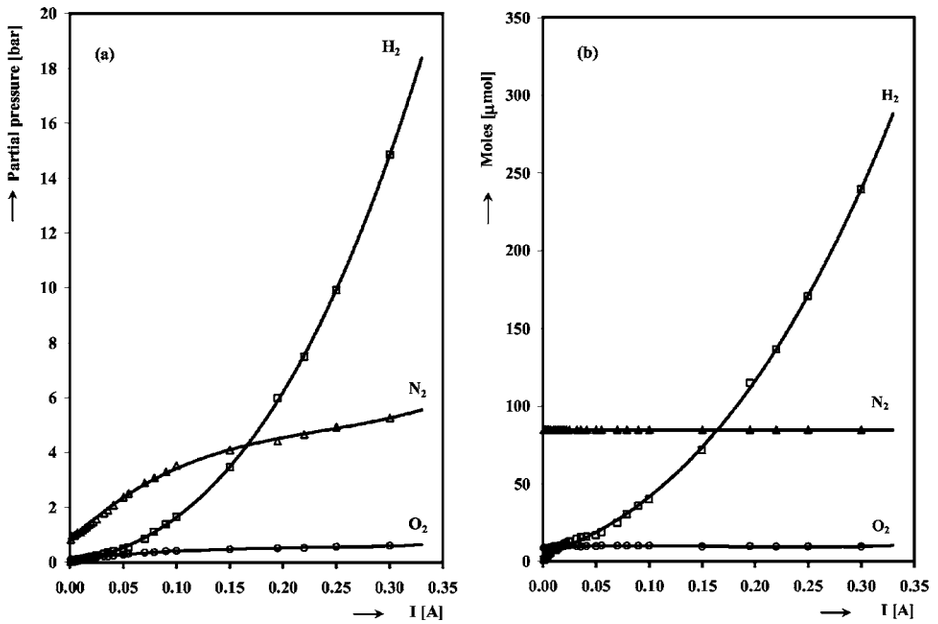

Figure 6. (a) Partial pressures of the analyzed gases. (b) Molar amounts of the analyzed gases.

$\theta \rightarrow 0$ and $\theta \rightarrow 1$) as was demonstrated for the case of the Heyrovsky step.[7,8,10] Third, when the free energy of adsorption becomes dependent on the surface coverage (when $0.2 < \theta < 0.8$), a change in the value of the Tafel slope may be observed.[8,45,46] A detailed study of the two possible mechanisms (Volmer-Heyrovsky and Volmer–Tafel) allowed the determination of the expected theoretical values of the Tafel slope corresponding to the three possible rds in the case of two adsorption isotherms; Langmuir and Temkin.[8,45] The predicted values of the Tafel slopes with a charge transfer coefficient of 0.5 are collected in Table II.

In our case, the Tafel slopes for region I are between 57 and 72 mV/dec. The Tafel slopes for the region II are between 114 and 144 mV/dec. In both regions the slope increases with temperature. Comparing these values to the theoretically predicted values in Table II, it can be concluded that the rds in the low current region is either the Heyrovsky or Tafel reaction and in the high current region the Volmer or Heyrovsky reaction. Because the first observation implies that the surface coverage is rather moderate or high in the low-current region I it is highly unlikely that the surface coverage will become lower at higher currents in region II. The Volmer reaction can therefore be excluded in region II and the Heyrovsky reaction is most likely the rds in the high-current region. To summarize, we have two possibilities for the rds: (*i*) the Heyrovsky reaction in the whole current range. As a result the change in the Tafel slope is due to a change in surface coverage and/or the free energy of adsorption and (*ii*) the Tafel reaction is rate-determining at low currents and the Heyrovsky reaction at high currents.

However, as pointed out by Erdey-Gruz et al.,[8] the specific shape of the polarization curves, constituting of two Tafel regions indicates whether the reaction steps are consecutive or parallel. In our case, the present shape excludes the possibility of two parallel reactions (Tafel and Heyrovsky). Consequently, the rds is most probably the Heyrovsky reaction in the entire current range and the change in the Tafel slope is attributed to the change in the free energy of adsorption with the surface coverage. In fact, at low currents the surface coverage is moderate and a Temkin isotherm is more suitable to describe it and at high currents the surface coverage is close to 1 so a Langmuir type isotherm is sufficient to describe it.

Arrhenius plots for the determined values of the exchange current at different temperatures revealed activation energy of 71 and 48 kJ/mol for region I and II, respectively (Fig. 8). A value of 56–58 kJ/mol activation energy was reported in the literature for the her with the Heyrovsky reaction as rds[13,47] and a value of about 80 kJ/mol was reported by Krstajic for the her on the Ni electrode[48] for the same rds (Heyrovsky). Usually the Tafel step is reported to have lower activation energy; about 34 kJ/mol.[48] The previously stated observations are in agreement with the rate-determining Heyrovsky reaction.

Expression of the her kinetics in case the Heyrovsky reaction is the rds.— For the Volmer-Heyrovsky mechanism, we have to consider Reactions 5 and 6. In case the free energy of adsorption does not depend on the surface coverage, these reactions have the following rate equations for the forward and backward directions

$$r_1 = K_1(1-\theta)\exp\left(-(1-\alpha_1)\frac{F}{RT}E\right) \qquad [35a]$$

$$r_{-1} = K_{-1}\theta\exp\left(\alpha_1\frac{F}{RT}E\right) \qquad [35b]$$

Table I. Kinetic parameters of the her at the Ni electrode.

	Region I			Region II			
T (°C)	b_{her} (mV/dec)	$I^{0,ref}_{her,ref}$ (10^{-6} A)	Activation energy (kJ/mol)	b_{her} (mV/dec)	$I^{0,ref}_{her,Ni}$ (10^{-4} A)	$1-\alpha_{her}$	Activation energy (kJ/mol)
10	57	2.53		114	3.40	0.493	
20	61	6.54		121	6.13	0.482	
30	66	21.70	71	128	12.59	0.470	48
40	69	45.50		136	22.57	0.457	
50	72	103.88		144	41.58	0.445	

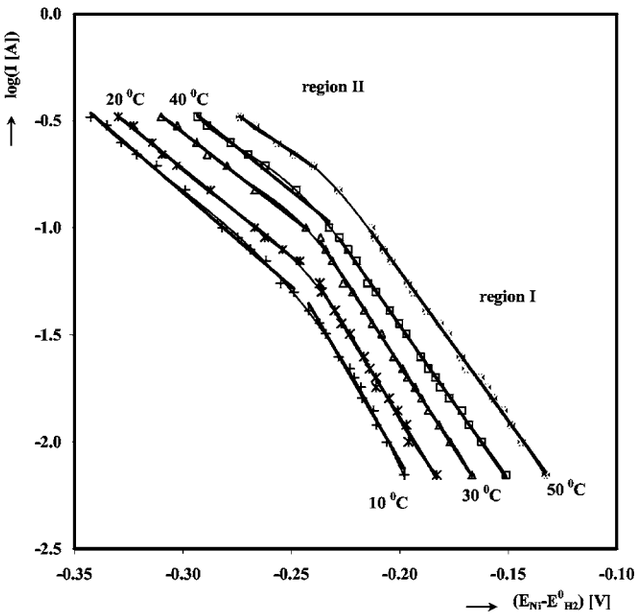

Figure 7. Polarization curves for the her at the Ni electrode.

$$r_2 = K_2\theta \exp\left(-(1-\alpha_2)\frac{F}{RT}E\right) \quad [35c]$$

$$r_{-2} = K_{-2}(1-\theta)p_{H_2} \exp\left(\alpha_2\frac{F}{RT}E\right) \quad [35d]$$

where E is the electrode potential versus a chosen reference electrode and K_j and K_{-j} are rate constants for the forward and backward directions. The partial currents for Reactions 1 and 2 are given by

$$I_1 = F(r_1 - r_{-1}) \quad [36]$$

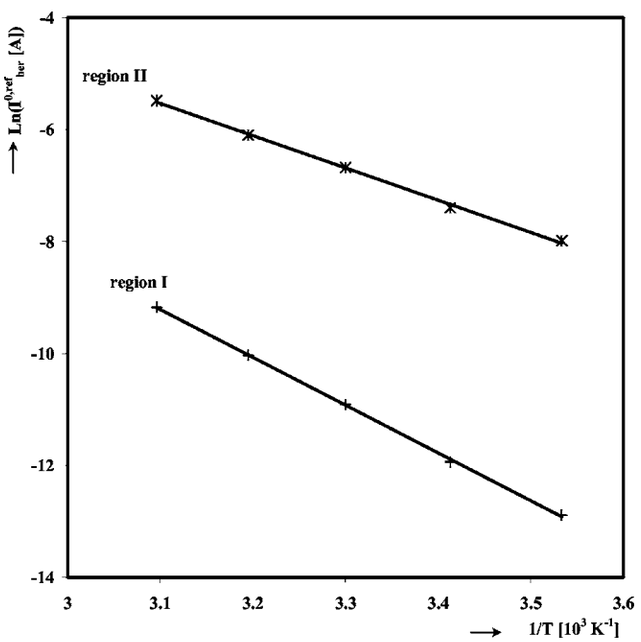

Figure 8. Arrhenius plots of the her exchange current in region I and II.

Table II. Predicted values of the Tafel slope for different rds of the her in both Langmuir and Temkin isotherm cases (the charge transfer coefficient is 0.5).

rds	Tafel slope (mV/dec) Langmuir isotherm $\theta \to 0$	Tafel slope (mV/dec) Temkin isotherm	Tafel slope (mV/dec) Langmuir isotherm $\theta \to 1$
Volmer	116	-	-
Heyrovsky	39	58	116
Tafel	29	58	∞

$$I_2 = F(r_2 - r_{-2}) \quad [37]$$

Under steady-state conditions, the hydrogen surface coverage does not change, i.e.

$$\frac{d\theta}{dt} = 0 = \frac{(I_1 - I_2)}{F} = (r_1 - r_{-1} - r_2 + r_{-2}) \quad [38]$$

which leads to $I_1 = I_2$. The charge balance gives the following equation

$$I_{her} = I_1 + I_2 = F(r_1 - r_{-1} + r_2 - r_{-2}) \quad [39]$$

Then, it is clear that

$$I_{her} = 2I_1 = 2I_2 \quad [40]$$

Replacing r_j and r_{-j} in Eq. 39 by using Eq. 35a–d, an expression for the hydrogen surface coverage as a function of potential is obtained. This equation gives the relationship between the steady state current and the electrode potential and involves 4 rate constants (K_j and K_{-j}, $j = 1, 2$) and two symmetry factors α_1 and α_2, so in total six parameters. This equation is rather complex to be practically useful and some simplifications are desirable.

One of the most important simplifications is to use the quasi-equilibrium assumption stating that all the steps prior to the rds are considered in equilibrium. Consequently, the rate of the forward reaction is almost equal to that of the backward reaction, so for the Volmer step; $r_1 \approx r_{-1}$. The surface coverage is then obtained from Eq. 35a and b

$$\theta = \frac{K_1}{K_{-1}\exp\left(\frac{F}{RT}E\right) + K_1} \quad [41]$$

Finally considering that for the rds $r_2 \gg r_{-2}$, the total current will be given by

$$I = 2Fr_2 \quad [42]$$

and the her current can be represented by

$$I_{her} = 2Fr_2 = 2FK_2\theta \exp\left(-(1-\alpha_2)\frac{F}{RT}E\right) = 2F\frac{K_1K_2 \exp\left(-(1-\alpha_2)\frac{F}{RT}E\right)}{K_{-1}\exp\left(\frac{F}{RT}E\right) + K_1} \quad [43]$$

In the limiting case when the coverage $\theta \to 1$, Eq. 43 reduces to

$$I_{her} = 2FK_2 \exp\left(-(1-\alpha_2)\frac{F}{RT}E\right) \quad [44]$$

and the Tafel slope becomes

$$b_{her} = \frac{2.3 \times RT}{(1 - \alpha_2)F} \quad [45]$$

which theoretically has a value of 116 mV/dec at 20°C for a symmetry factor of 0.5.

For intermediate values of coverage, especially around a surface coverage of 0.5, the free energy of adsorption is a function of the coverage due to the nonuniformity of the surface and the Langmuir isotherm is no longer valid and either a Frumkin type or a Temkin type of isotherm should be considered.[8,45,46] For a Temkin type of isotherm, Eq. 35a–c will be transformed into[46]

$$r_1 = K_1(1 - \theta)\exp\left(-(1 - \alpha_1)\frac{F}{RT}E\right)\exp\left(\frac{(1 - \gamma)\theta}{RT}\frac{d\Delta G_\theta^0}{d\theta}\right) \quad [46a]$$

$$r_{-1} = K_{-1}\theta \exp\left(\alpha_1\frac{F}{RT}E\right)\exp\left(\frac{-\gamma\theta}{RT}\frac{d\Delta G_\theta^0}{d\theta}\right) \quad [46b]$$

$$r_2 = K_2\theta \exp\left(-(1 - \alpha_2)\frac{F}{RT}E\right)\exp\left(\frac{(1 - \gamma)\theta}{RT}\frac{d\Delta G_\theta^0}{d\theta}\right) \quad [46c]$$

where γ is a symmetry factor for the adsorption process and $\theta\frac{d\Delta G_\theta^0}{d\theta}$ is the change of the free energy of adsorption as a function of θ.

At intermediate coverages (around 0.5), the change of the exponential terms in the above expressions with θ is more important than that of the pre-exponential terms and these equations can therefore be simplified to

$$r_1 \approx K_1'\exp\left(-(1 - \alpha_1)\frac{F}{RT}E\right)\exp\left(\frac{(1 - \gamma)\theta}{RT}\frac{d\Delta G_\theta^0}{d\theta}\right) \quad [47a]$$

$$r_{-1} \approx K_{-1}'\exp\left(\alpha_1\frac{F}{RT}E\right)\exp\left(\frac{-\gamma\theta}{RT}\frac{d\Delta G_\theta^0}{d\theta}\right) \quad [47b]$$

$$r_2 \approx K_2'\exp\left(-(1 - \alpha_2)\frac{F}{RT}E\right)\exp\left(\frac{(1 - \gamma)\theta}{RT}\frac{d\Delta G_\theta^0}{d\theta}\right) \quad [47c]$$

where K_1', K_{-1}', and K_2' are redefined constants. Again, assuming a quasi-equilibrium state, Eq. 47a and b are equal which leads to

$$\exp\left(\frac{\theta}{RT}\frac{d\Delta G_\theta^0}{d\theta}\right) = \frac{K_{-1}'}{K_1'}\exp\left(-\frac{F}{RT}E\right) \quad [48]$$

Introducing this equation in the expression for the rate of Reaction 2 (Eq. 47c) yields

$$r_2 \approx K_2^T\exp\left((-2 + \gamma + \alpha_2)\frac{F}{RT}E\right) \quad [49]$$

and

$$I_{her} = 2Fr_2 \approx 2FK_2^T\exp\left((-2 + \gamma + \alpha_2)\frac{F}{RT}E\right) \quad [50]$$

where

$$K_2^T = K_2'\left(\frac{K_{-1}'}{K_1'}\right)^{1-\gamma}$$

Hence the Tafel slope is

$$b_{her} = \frac{2.3 \times RT}{(2 - \gamma - \alpha_2)F} \quad [51]$$

Taking $\alpha_2 = \gamma = 0.5$, the Tafel slope should be 58 mV/dec at 20°C. This value is in agreement with the obtained Tafel slopes in region I. This explains the appearance of the two Tafel slopes and confirms the result that the her proceeds more likely via the Volmer-Heyrovsky mechanism with the Heyrovsky reaction as rds.

To obtain the charge transfer coefficients ($\alpha_2 = \alpha_{her}$) at different temperatures, only the high current region, for which the Tafel slope is expressed by Eq. 45, is used as the exact value for γ is unknown. The corresponding values are listed in Table I. It was found that the obtained charge transfer coefficient increases as the temperature increases from 0.507 at 10°C to 0.555 at 50°C. This behavior was discussed by Conway et al.[49] and assumed to be due to the contribution of a temperature-independent enthalpic term (β_H) and a temperature-dependent entropic term ($\beta_S T$), where $\beta_2 = 1 - \alpha_2$ can be written as

$$\beta_2 = \beta_H + \beta_S T \quad [52]$$

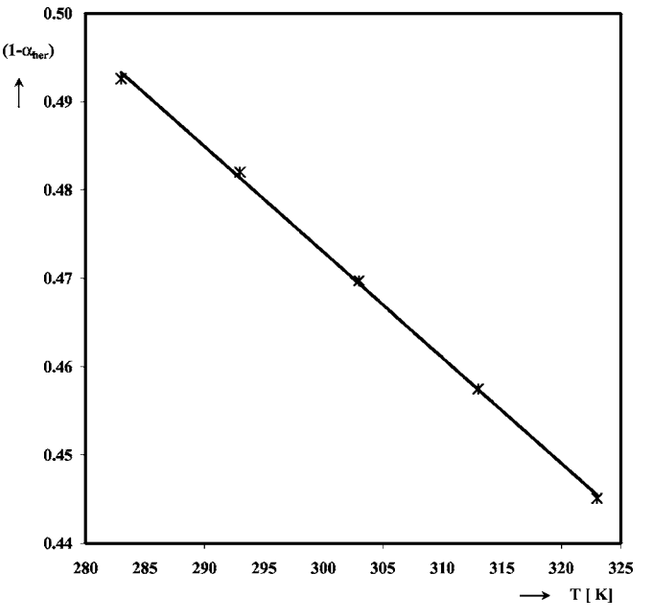

Figure 9. Dependency of the charge transfer coefficient on the temperature for the her at the Ni electrode.

Plotting $(1 - \alpha_2)$ in region II as a function of temperature (Fig. 9), reveals that Eq. 52 is perfectly satisfied with $\beta_H = 0.83$ and $\beta_S = -1.20 \times 10^{-3}$ K^{-1}. These values are close to those obtained by Krstajic for the her at nickel electrode in alkaline solution ($\beta_H = 0.87$ and $\beta_S = -1.31 \times 10^{-3}$ K^{-1})[48] and by Vracar for the Pd-Ni electrode ($\beta_H = 0.9$ and $\beta_S = -1.53 \times 10^{-3}$ K^{-1}).[50]

The hydrogen oxidation reaction (hor).— Figure 10 shows the battery internal gas pressure increase during steady-state overdischarging at different temperatures. The pressure buildup is very pronounced especially at low temperature. For example, it causes the safety vent to open at a discharging current of 0.22 A at 10°C. This demonstrates, on the one hand, how important it is to improve and control the hydrogen oxidation properties of the MH electrode and, on the other hand, the necessity to investigate the electrodes expansion affecting the free gas volume inside the battery.

In Fig. 11, one can see the relationship between the overdischarging current and the partial hydrogen pressure at the different temperatures. For all temperatures and considering the experimented current range, the relationship between the overdischarging current and the hydrogen partial pressure is not linear and Eq. 33 is not satisfied. So a complete diffusion controlled reaction is not the case for the hor at the MH electrode.

To investigate the kinetics of the hor in more detail, Eq. 30 was considered. In Fig. 12a, $\ln I_{hor,MH} - \left(\alpha_{hor}\frac{nF}{RT}(E_{MH} - E_{H_2}^0(T))\right)$ (α_{hor} is considered equal to 0.5) is plotted against $\ln\left(\frac{P_{H_2}}{P_{H_2,ref}}\right)$ for the different temperatures. It can be seen that straight lines with almost equal slopes of 0.5, representing the reaction order for H_2, are obtained at 10 and 20°C. At higher temperatures a deviation of the slope to lower values is observed. This deviation could be due to the fact that

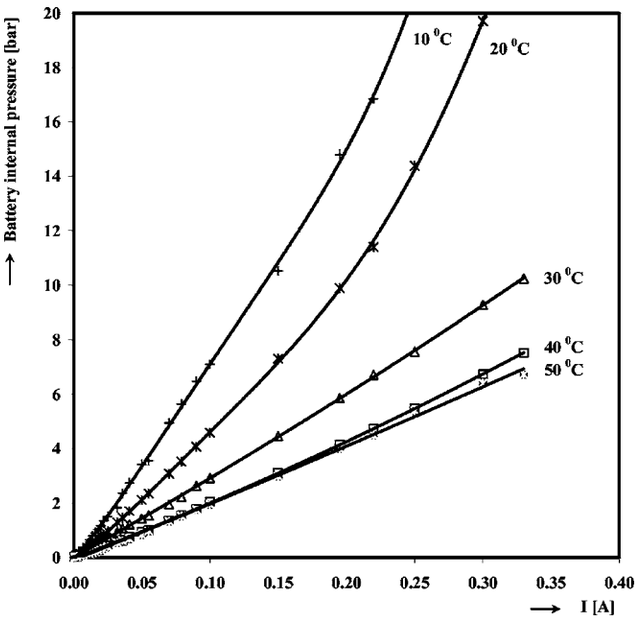

Figure 10. Measurement of the internal pressure increase inside sealed NiMH battery during steady-state overdischarge at different temperatures.

the charge transfer coefficient is not constant but temperature-dependent. An optimization of the values of α_{hor} at the different temperatures showed that, indeed, α_{hor} is dependent on the temperature. Figure 12b shows the same curves as Fig. 12a, using the optimized values of α_{hor}. It is clear from these curves that the reaction order is 0.5 at all temperatures and that the hor kinetics perfectly obeys Eq. 30.

Figure 13 shows the optimized charge transfer coefficients (α_{hor}) dependency on temperature. A Conway-type of relationship is observed with an enthalpic constant of 1.47 and an entropic constant of $-3.34 \cdot 10^{-3}$ K^{-1} (see Eq. 52). These results confirm the hypothesis

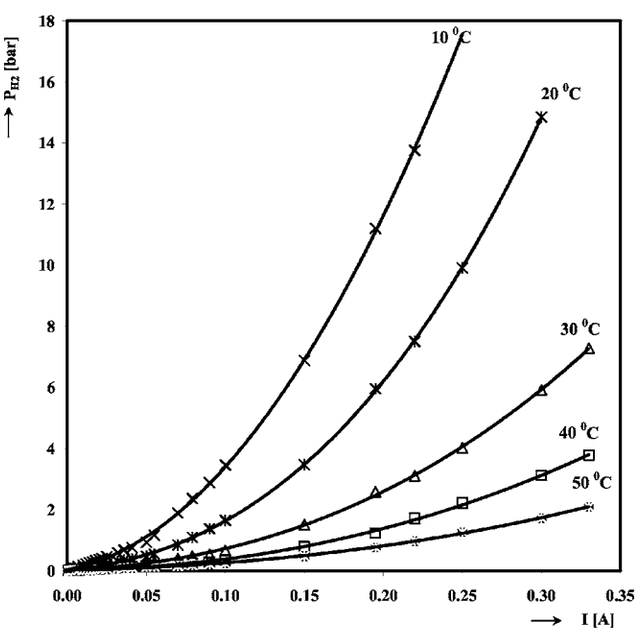

Figure 11. The hydrogen partial pressure as a function of the overdischarge current at different temperatures.

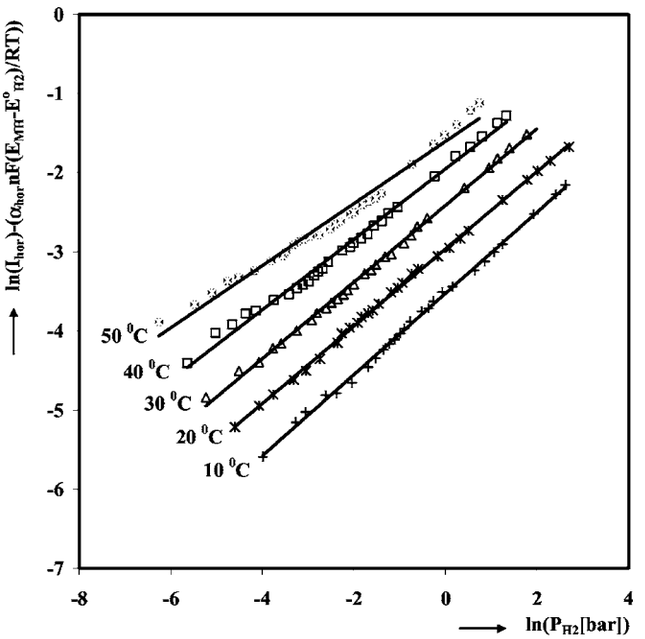

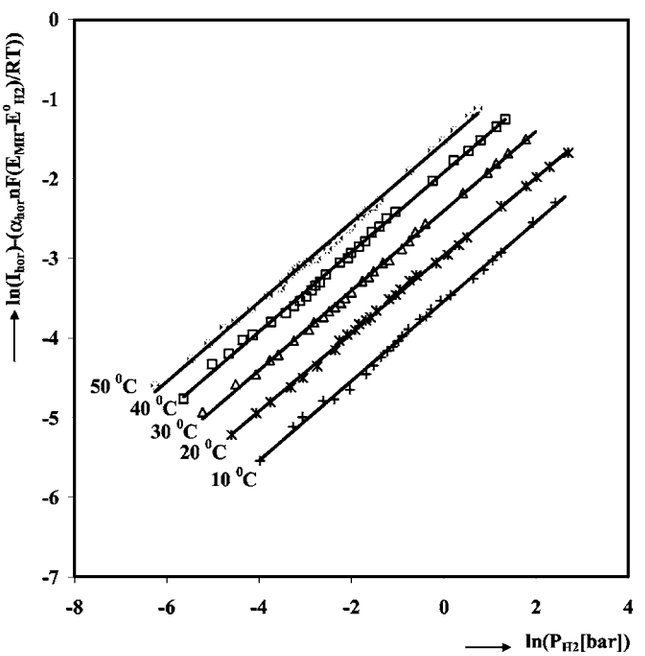

Figure 12. (a) The kinetics of the hor: $\ln I_{hor,MH} - \left(\alpha_{hor}\frac{nF}{RT}(E_{MH} - E^0_{H_2}(T))\right)$ plotted against $\ln\left(p_{H_2}/P_{H_2,ref}\right)$ for α_{hor} equal to 0.5. (b) The kinetic of the hor: $\ln I_{hor,MH} - \left(\alpha_{hor}nF/RT(E_{MH} - E^0_{H_2}(T))\right)$ plotted against $\ln\left(p_{H_2}/P_{H_2,ref}\right)$ for optimized values of α_{hor}.

of a kinetically controlled hor. However, it is not wise to generalize this conclusion outside the investigated current range where the observed overpotential at the MH electrode was found to be relatively low. For higher overpotentials, diffusion limitations may occur.[36-41] This was indeed experimentally observed at a MH electrode, when its capacity decreases because loss of active material. For such degraded electrode, the potential jumps to high values corresponding to the oxygen evolution reaction (oer) region. This demonstrates the existence of limiting current region corresponding to the hor before the oer starts to occur. This aspect is not discussed in detail here due

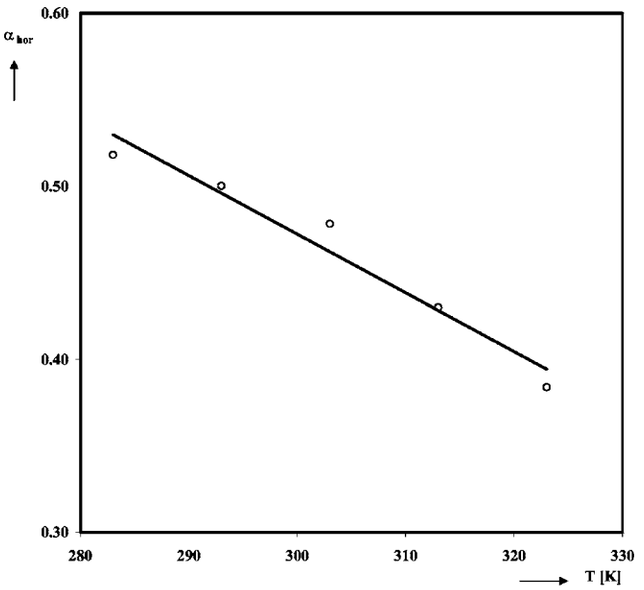

Figure 13. Optimized values for α_{hor} as a function of temperature.

to the impossibility of controlling the capacity loss and the probable opening of the safety vent which affects the reproducibility of the experiments at currents higher than 0.33 A.

The exchange current for the hor at the MH electrode $I^{0,ref}_{hor,MH}$, was determined and found to be in the milliampere order of magnitude. These high values indicate facile kinetics compared to the her in region I [for which the exchange current is in the microampere order of magnitude (see Table II)]. From the Arrhenius plot (Fig. 14)) of the hor exchange current, activation energy of 38 kJ/mol was determined. The kinetic parameters of the hor are all collected in Table III.

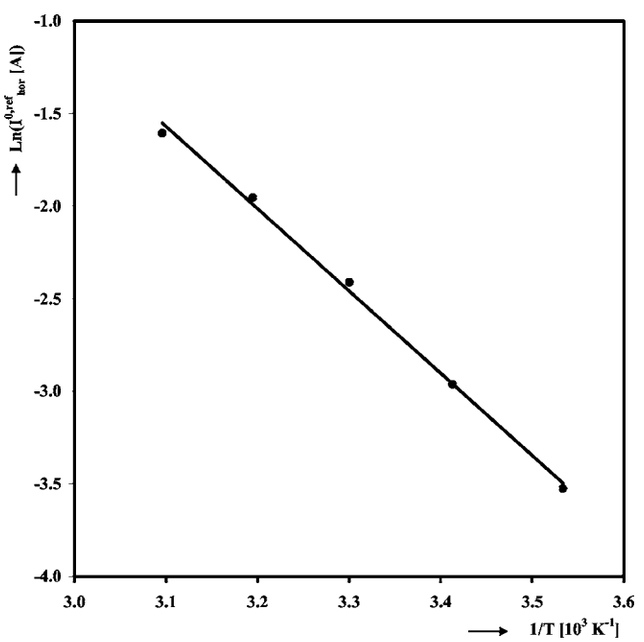

Figure 14. Arrhenius plot of the hor exchange current.

Table III. Kinetic parameters of the hor at the MH electrode.

T (°C)	$I^{0,ref}_{hor,MH}$ (mA)	α_{hor}	Reaction order	Activation energy (kJ/mol)
10	29.0	0.52	0.5	
20	51.6	0.50	0.5	
30	90.5	0.48	0.5	38
40	146.4	0.43	0.5	
50	212.6	0.38	0.5	

Conclusions

The utilization of in situ gas phase analyses combined with the electrochemical investigation of the hydrogen evolution reaction (her) and the hydrogen oxidation reaction (hor) in commercial NiMH batteries provided essential information on the kinetics of these reactions under real battery operation conditions. It was shown that the generation of hydrogen is the most dominant process during overdischarge of NiMH batteries especially at low temperatures even at very low discharging currents. More precautions have to be taken when using these batteries in series as different batteries have slightly different capacities, inducing the battery with the lowest capacity to be overdischarged. Hence, the her takes place in NiMH batteries, inducing the internal gas pressure to climb to very high values, even beyond the critical pressures at which the safety vents of these batteries open.

The kinetic investigations of the her confirmed the occurrence of a Volmer-Heyrovsky mechanism with the Heyrovsky step as rds. Two well-defined Tafel regions were found, with representative Tafel slopes, 60 and 120 mV/dec at 20°C, for the low and high current regions, respectively. The lower Tafel slope shows that the Langmuir isotherm is not sufficient to describe the surface coverage with the adsorbed hydrogen atoms. In that case, a Temkin type isotherm gives a better description. The corresponding activation energies for the low and high current regions are 71 and 48 kJ/mol, respectively. The exchange current was found to be 2 orders of magnitude higher at high currents than that at low currents. For example, at 20°C, it is $6.54 \cdot 10^{-6}$ A for the low η region and 6.13×10^{-4} A for the high η region. A Conway-type linear dependency of the charge transfer coefficient with temperature was observed.

The hor was found to be kinetically controlled in the investigated current range. The reaction order toward hydrogen was found to be 0.5 and the determined charge transfer coefficient was found to be linearly dependent on temperature. The activation energy of the hor is about 38 kJ/mol.

Eindhoven University of Technology assisted in meeting the publication costs of this article.

References

1. K. Hong, *J. Alloys Compd.*, **321**, 307 (2001).
2. T. Takamura, *Solid State Ionics*, **152-153**, 19 (2002).
3. M. Ikoma, *Enerug Shigen*, **19**, 233 (1998).
4. M. Ikoma and N. Fujioka, *Kagaku to Kogyo (Tokyo)*, **49**, 213 (1998).
5. P. H. L. Notten, in *Interstitial Intermetallic Alloys*, F. Grandjean, G. J. Long, and K. H. J. Buschow, Editors, p. 151, Kluwer Academic Publishers, London (1995).
6. P. H. L. Notten and J. R. G. van Beek, *Hemijska Industrija*, **54**, 102 (2000).
7. D. Pletcher, *A First Course in Electrode Processes*, Alresford Press Ltd, England (1991).
8. T. Erdey-Gruz, *Kinetics of Electrode Processes*, Adam Hilger Ltd., London (1972).
9. J. O'M. Bockris and E. C. Potter, *J. Electrochem. Soc.*, **99**, 169 (1952).
10. P. A. Christensen, and A. Hamnett, *Techniques and Mechanisms in Electrochemistry*, Blackie Academic and Professional, London (1993).
11. A. C. Chialvo and M. R. Gennero de Chialvo, *J. Appl. Electrochem.*, **21**, 440 (1991).
12. J. R. C. Salgado, M. H. S. Andrade, J. C. P. Silva, and J. Tonholo, *Electrochim. Acta*, **47**, 1997 (2002).
13. A. N. Correia and S. A. S. Machado, *Electrochim. Acta*, **43**, 367 (1997).
14. J. P. Diard, B. LeGorrec, and S. Maximovitch, *Electrochim. Acta*, **35**, 1099 (1990).
15. N. Krstajic, M. Popovic, B. Grgur, M. Vojnovic, and D. Sepa, *J. Electroanal. Chem.*, **512**, 16 (2001).
16. A. N. Correia, S. A. S. Machado, and L. A. Avaca, *Electrochem. Commun.*, **1**, 600

(1999).
17. L. Vracar, S. Burojevic, and N. Krstajic, *J. Serb. Chem. Soc.*, **63**, 201 (1998).
18. N. A. Assuncao, M. J. De Giz, G. Tremiliosi-Filho, and E. R. Gonzalez, *J. Electrochem. Soc.*, **144**, 2794 (1997).
19. S. S. Buttarello, G. Tremiliosi-Filho, and E. R. Gonzalez, *Electrochemistry and Materials Science of Cathodic Hydrogen Absorption and Adsorption*, B. E. Conway and G. Jerkiewicz, Editors, PV 94-21, p. 299, The Electrochemical Society Proceedings Series, Pennington, NJ (1994).
20. M. J. De Giz, G. Tremiliosi-Filho, and E. R. Gonzalez, *Electrochim. Acta*, **39**, 1775 (1994).
21. M. A. V. Devanathan and M. Selvaratnam, *Trans. Faraday Soc.*, **56**, 1820 (1960).
22. B. E. Conway, *Sci. Prog.*, **71**, 479 (1987).
23. D. Luo, W. Hu, Y. Wang, Y. Zhang, and G. Wang, *J. Mater. Sci. Technol.*, **12**, 190 (1996).
24. E. R. Gonzalez, L. A. Avaca, G. Tremiliosi-Filho, S. A. S. Machado, and M. Ferreira, *Int. J. Hydrogen Energy*, **19**, 17 (1994).
25. M. J. Giz, M. C. Marengo, E. A. Ticianelli, and E. R. Gonzalez, *Ecletica Quim.*, **28**, 21 (2003).
26. R. Notoya, *Electrochim. Acta*, **42**, 899 (1996).
27. M. F. Kibria, M. Sh Mridha, and A. H. Kha, *Int. J. Hydrogen Energy*, **20**, 435 (1995).
28. A. C. D. Angelo and A. Lasia, *J. Electrochem. Soc.*, **142**, 3313 (1995).
29. K. K. Lian and V. I. Birss, *J. Electrochem. Soc.*, **138**, 2885 (1991).
30. A. N. Correia, S. A. S. Machado, and L. A. Avaca, *Electrochem. Commun.*, **1**, 600 (1999).
31. T. Benameur, R. Yavari, and R. Durand, *Mater. Sci. Eng., A*, **181**, 1145 (1994).
32. K. M. S. Huq and A. J. Rosenberg, *J. Electrochem. Soc.*, **111**, 270 (1964).
33. N. A. Assuncao, M. J. De Giz, G. Tremiliosi-Filho, and E. R. Gonzalez, *J. Electrochem. Soc.*, **144**, 2794 (1997).
34. A. Matsuda, R. Notoya, T. Ohmori, K. Kunimatsu, and T. Kushimoto, *J. Res. Inst. Catal.*, **24**, 187 (1976).
35. N. Krstajic, M. Popovic, B. Grgur, M. Vojnovic, and D. Sepa, *J. Electroanal. Chem.*, **512**, 16 (2001).
36. J. O'M. Bockris and H. Mauser, *Can. J. Chem.*, **37**, 475 (1959).
37. A. Lasia, *J. Electroanal. Chem.*, **454**, 115 (1998).
38. B. E. Conway and B. V. Tilak, *Electrochim. Acta*, **47**, 3571 (2002).
39. M. R. Gennero de Chialvo, and A. C. Chialvo, *Phys. Chem. Chem. Phys.*, **6**, 4009 (2004).
40. P. M. Quaino, M. R. Gennero de Chialvo, and A. C. Chialvo, *Phys. Chem. Chem. Phys.*, **6**, 4450 (2004).
41. F. Alcaide, E. Brillas, and P.-L. Cabot, *J. Electrochem. Soc.*, **152**, E319 (2005).
42. P. H. L. Notten, E. Verbitskiy, W. S. Kruijt, and H. J. Bergveld, *J. Electrochem. Soc.*, **152**, A1423 (2005).
43. M. C. Lefebvre, in *Modern Aspects of Electrochemistry*, 32nd ed., B. E. Conway, J. O'M. Bockris, and R. E. White, Editors, p. 249, Kluwer Academic/Plenum Publishers, New York (1999).
44. A. J. G. Mank, A. Belfadhel-Ayeb, P. V. E. Kruesemann, and P. H. L. Notten, *Appl. Spectrosc.*, **59**, 109 (2005).
45. B. E. Conway and M. Salmon, *Electrochim. Acta*, **9**, 1599 (1964).
46. B. V. Tilak and B. E. Conway, *Electrochim. Acta*, **37**, 51 (1992).
47. S. A. S. Machado and L. A. Avaca, *Electrochim. Acta*, **39**, 1385 (1994).
48. N. Krstajic, M. Popovic, B. Grgur, M. Vojnovic, and D. Sepa, *J. Electroanal. Chem.*, **512**, 27 (2001).
49. B. E. Conway, D. F. Tessier, and D. P. Wilkinson, *J. Electrochem. Soc.*, **136**, 2486 (1989).
50. L. Vracar, S. Burojevic, and N. Krstajic, *J. Serb. Chem. Soc.*, **63**, 201 (1998).